Asymptotic Scaling and Infrared Behavior of the Gluon Propagator

Derek B. Leinweber, Jon Ivar Skullerud* and Anthony G. Williams

Special Research Centre for the Subatomic Structure of Matter and Department of Physics and Mathematical Physics, University of Adelaide, Adelaide SA 5005, Australia

Claudio Parrinello*

Department of Mathematical Sciences, University of Liverpool, Liverpool L69 3BX, England

Abstract

The Landau gauge gluon propagator for the pure gauge theory is evaluated on a $32^3 \times 64$ lattice with a physical volume of $(3.35^3 \times 6.7)$ fm^4. Comparison with two smaller lattices at different lattice spacings allows an assessment of finite volume and finite lattice spacing errors. Cuts on the data are imposed to minimize these errors. Scaling of the gluon propagator is verified between $\beta = 6.0$ and $\beta = 6.2$. The tensor structure is evaluated and found to be in good agreement with the Landau gauge form, except at very small momentum values, where some small finite volume errors persist. A number of functional forms for the momentum dependence of the propagator are investigated. The form $D(q^2) = D_{\mathrm{IR}} + D_{\mathrm{UV}}$, where $D_{\mathrm{IR}}(q^2) \propto (q^2 + M^2)^{-\eta}$ and D_{UV} is an infrared regulated one-loop asymptotic form, is found to provide an adequate description of the data over the entire momentum region studied — thereby bridging the gap between the infrared confinement region and the ultraviolet asymptotic region. The best estimate for the exponent η is $3.2^{+0.1+0.2}_{-0.2-0.3}$, where the first set of errors represents the uncertainty associated with varying the fitting range, while the second set of errors reflects the variation arising from different choices of infrared regulator in D_{UV}. Fixing the form of D_{UV}, we find that the mass parameter M is (1020 ± 100) MeV.

---

*UKQCD Collaboration

I. INTRODUCTION

Over the years, the infrared behavior of the gluon propagator has been studied using a variety of approaches, and with widely differing results. Gribov [1] argued that by restricting the functional integral to eliminate gauge copies, one would obtain a gluon propagator which vanishes in the infrared. Stingl [2] found that this solution was consistent with the gluon Dyson–Schwinger equation (DSE), when ignoring the 4-gluon vertex and placing certain restrictions on the remaining vertices. Recent studies of the coupled ghost and gluon DSEs [3,4] support this conclusion, in principle if not in detail. On the other hand, DSE studies of the gluon self-energy [5–7] (ignoring the role of ghosts) have resulted in a gluon propagator which is strongly enhanced in the infrared. Occupying the 'middle ground' between these positions, Cornwall [8] has used a gauge invariant 'pinch technique' DSE to obtain a dynamical gluon mass. For a recent review of DSEs, see Ref. [9].

The infrared behavior of the gluon propagator is often considered to be crucial to confinement. Both the infrared-vanishing and the infrared-enhanced solutions have been argued to provide mechanisms for confinement. It has even been argued [10] that an infrared-enhanced gluon propagator is a *necessary* condition for confinement. Clearly then, a settlement of this issue should allow us to shed some light on the problem of confinement.

Lattice field theory provides a model-independent, *ab initio* approach to QCD, and can in principle answer this question. However, previous lattice studies of the gluon propagator in Landau gauge [11,12] have been inconclusive. The reason for this is that the lowest non-trivial momentum value accessible on a finite lattice is inversely proportional to the length of the box. The region of interest is likely to be below 1 GeV. Ref. [12] used a lattice with a spatial length of 2.5 fm and a length of 5 fm in the time direction, giving access in principle to momentum values down to 250 MeV. However, finite volume effects could be shown to be significant at least up to approximately 500 MeV on this lattice, thereby casting doubt on the validity of the results in the infrared. In this study we increase the lattice size to 3.35 fm in the spatial directions and 6.7 fm in the time direction, giving access to momenta deeper in the infrared and significantly reducing finite volume effects. Preliminary results can be found in Ref. [13]. We have also compared the results for this lattice to those obtained on a smaller volume and used anisotropies in the data to assess finite volume effects. However, an extrapolation to infinite volume has not been attempted.

The structure of this paper is as follows: In Section II we present our method for calculating the gluon propagator on the lattice, as well as the notation we use. The details of our simulations are given in Section III. In Section IV we discuss how to handle finite volume and finite lattice spacing artefacts. The majority of our results can be found in Section V. Section V A discusses the tensor structure; in Section V B the asymptotic behavior is studied; and in Section V C we fit the gluon propagator as a function of momentum to various functional forms. Finally, in Section VI we discuss the significance of our results.

II. THE GLUON PROPAGATOR ON THE LATTICE

A. Definitions and notation

The gauge links $U_\mu(x) \in \mathrm{SU}(3)$ may be expressed in terms of the continuum gluon fields as

$$U_\mu(x) = \mathcal{P} e^{ig_0 \int_x^{x+\hat{\mu}} A_\mu(z)dz} = e^{ig_0 a A_\mu(x+\hat{\mu}/2)} + \mathcal{O}(a^3) \,. \tag{2.1}$$

where $\mathcal{P}$ denotes path ordering. From this, the dimensionless lattice gluon field $A_\mu^L(x)$ may be obtained via

$$A_\mu^L(x + \hat{\mu}/2) = \frac{1}{2ig_0}\left(U_\mu(x) - U_\mu^\dagger(x)\right) - \frac{1}{6ig_0}\mathrm{Tr}\left(U_\mu(x) - U_\mu^\dagger(x)\right) \,, \tag{2.2}$$

which is accurate to $\mathcal{O}(a^2)$. The discrete momenta $\hat{q}$ available on a finite, periodic volume of length L_μ in the μ direction, are given by

$$\hat{q}_\mu = \frac{2\pi n_\mu}{aL_\mu}, \qquad n_\mu = 0, \ldots, L_\mu - 1 \,. \tag{2.3}$$

The momentum space gluon field is

$$A_\mu(\hat{q}) \equiv \sum_x e^{-i\hat{q}\cdot(x+\hat{\mu}/2)} A_\mu^L(x + \hat{\mu}/2)$$
$$= \frac{e^{-i\hat{q}_\mu a/2}}{2ig_0}\left[\left(U_\mu(\hat{q}) - U_\mu^\dagger(-\hat{q})\right) - \frac{1}{3}\mathrm{Tr}\left(U_\mu(\hat{q}) - U_\mu^\dagger(-\hat{q})\right)\right], \tag{2.4}$$

where $U_\mu(\hat{q}) \equiv \sum_x e^{-i\hat{q}x} U_\mu(x)$, $A_\mu(\hat{q}) \equiv t^a A_\mu^a(\hat{q})$, and t^a are the generators of the SU(3) Lie algebra. This definition differs by a term of $\mathcal{O}(a)$ from the one usually found in the literature, where $U_\mu(x) = \exp(ig_0 A'_\mu(x))$, which gives $A'_\mu(\hat{q}) = \exp(i\hat{q}_\mu a/2)A_\mu(\hat{q}) = A_\mu(\hat{q}) + \mathcal{O}(a)$. The dimensionless lattice gluon propagator $D_{\mu\nu}^{L,ab}(\hat{q})$ is defined by

$$\langle A_\mu^a(\hat{q}) A_\nu^b(-\hat{q}')\rangle = V\delta(\hat{q} - \hat{q}')D_{\mu\nu}^{L,ab}(\hat{q})\,, \tag{2.5}$$

where V is the lattice volume.

The continuum, infinite-volume gluon propagator in a covariant gauge with gauge parameter ξ has the form

$$D_{\mu\nu}^{ab}(q) = (\delta_{\mu\nu} - \frac{q_\mu q_\nu}{q^2})\delta^{ab} D(q^2) + \xi\frac{q_\mu q_\nu}{q^2}\delta^{ab}\frac{1}{q^2} \,. \tag{2.6}$$

The scalar function $D(q^2)$ can be extracted from $D_{\mu\nu}^{ab}(q)$ by

$$D(q^2) = \frac{1}{3}\left(\left[\sum_\mu \frac{1}{8}\sum_a D_{\mu\mu}^{aa}(q)\right] - \frac{\xi}{q^2}\right) \,. \tag{2.7}$$

This expression is also valid on a finite volume, provided q is not too close to zero. The finite volume induces an effective 'mass' $m \sim 1/L$ which becomes significant for q sufficiently close to 0. In this case, the most general form possible for the tensor structure is

$$D_{\mu\nu}^{ab}(q) = \left(\delta_{\mu\nu} - \frac{h_{\mu\nu}(q)}{f(q^2)}\right)\delta^{ab}D(q^2) + \xi\delta^{ab}\frac{h'_{\mu\nu}(q)}{g(q^2)}, \tag{2.8}$$

where, $f(q^2) \to q^2$, $g(q^2) \to q^4$, and $h_{\mu\nu}$ and $h'_{\mu\nu} \to q_\mu q_\nu$ for sufficiently large q, but $f(q^2)$ and $g(q^2)$ go to finite values for $q = 0$. In the following, we will work in the Landau gauge, $\xi = 0$, and we will only attempt fits to lattice data for which finite size effects can be shown to be small.

A well-known lattice artefact is that the tree level propagator of a massless scalar boson field does not reproduce the expected continuum result of

$$D^{(0)}(q^2) = \frac{1}{q^2}, \tag{2.9}$$

but rather produces

$$D^{(0)}(\hat{q}) = \frac{1}{\sum_\mu (\frac{2}{a}\sin\hat{q}_\mu a/2)^2}. \tag{2.10}$$

Since QCD is asymptotically free, we expect that $q^2 D(q^2) \to 1$ up to logarithmic corrections as $q^2 \to \infty$. To ensure this result we work with a momentum variable defined as[1]

$$q_\mu \equiv \frac{2}{a}\sin\frac{\hat{q}_\mu a}{2}. \tag{2.11}$$

In the infrared region of greatest interest, the choice of q vs. $\hat{q}$ makes little difference in the results.

B. Renormalization

The bare, dimensionless lattice gluon propagator $D^L(qa)$ is related to the renormalized continuum propagator $D_R(q;\mu)$ via

$$a^2 D^L(qa) = Z_3(\mu, a)D_R(q;\mu). \tag{2.12}$$

The renormalization constant $Z_3(\mu, a)$ is determined by imposing a renormalization condition at some chosen renormalization scale μ, eg.,

$$D_R(q)|_{q^2=\mu^2} = \frac{1}{\mu^2}. \tag{2.13}$$

The renormalized gluon propagator can be computed both non-perturbatively on the lattice and perturbatively in the continuum for choices of the renormalization point in the ultraviolet. It can then be related to the propagator in other continuum renormalization schemes, such as $\overline{\text{MS}}$.

---

[1] The momenta q and $\hat{q}$ are often defined the other way around in the lattice literature. However, we feel it is more instructive here to define q as above, such that lattice results reproduce the continuum formula (2.6) and the tree level formula (2.9).

C. Gauge fixing

The lattice implementation of the Landau gauge is based on a variational principle. In continuum language, this can be seen by defining for any generic field configuration $A_\mu(x)$ the following functional on the group of gauge transformations:

$$F_A^c[g] = \| A^g \|^2 = \int d^4x \mathrm{Tr}\, (A_\mu^g(x))^2, \tag{2.14}$$

where

$$A_\mu^g(x) = g^{-1}(x)A_\mu(x)g(x) - g^{-1}(x)\partial_\mu g(x) \qquad g(x) \in \mathrm{SU}(3). \tag{2.15}$$

By considering gauge transformations of the form

$$g'(x) = g(x)e^{i\omega(x)} = g(x)e^{it^a \omega^a(x)} \tag{2.16}$$

and expanding to second order in ω, it can be shown that

$$F_A^c[g'] = F_A^c[g] - 2i \int d^4x \mathrm{Tr}\, (A_\mu^g(x)\partial_\mu \omega(x)) - \int d^4x \mathrm{Tr} \sum_a \omega^a(x)(O[A^g]\omega)^a(x) + \mathcal{O}(\omega^3). \tag{2.17}$$

This implies that $F_A^c[g]$ is stationary when $A_\mu^g(x)$ satisfies the Landau gauge condition $\partial \cdot A^g = 0$. If A^g is in the Landau gauge, the operator appearing in the quadratic term of Eq. (2.17) is $O[A^g] \equiv FP[A^g]$, i.e. the Faddeev–Popov operator in the Landau gauge:

$$(FP[A^g])_{xy}^{ab} = - \left(\partial \cdot \partial\, \delta^{ab} + f^{abc} A_\mu^{gc}(x)\partial_\mu \right) \delta^4(x - y). \tag{2.18}$$

Since configurations corresponding to local minima of $F_A^c[g]$ satisfy the gauge condition, Landau gauge fields may be constructed from a generic configuration $A_\mu(x)$ by minimizing $F_A^c[g]$. This can be implemented in a quite straighforward way on the lattice: a suitable discretization of $F_A^c[g]$ is given by

$$F_U^L[g] = 1 - \sum_{\mu,x} \mathrm{Re\, Tr}\, U_\mu^g(x), \tag{2.19}$$

where

$$U_\mu^g(x) = g(x)U_\mu(x)g^\dagger(x + \hat\mu). \tag{2.20}$$

$F_U^L[g]$ can be minimized numerically (for a review, see Ref. [14]), and the resulting link configurations satisfy

$$\theta = \frac{1}{VN_c} \sum_x \theta(x) = \frac{1}{VN_c} \sum_x \mathrm{Tr}\, (\Delta(x)\Delta^\dagger(x)) = 0 \tag{2.21}$$

where $\Delta(x)$ is the lattice four-divergence of the gluon field,

5

$$\Delta(x) = \sum_\mu \left(A_\mu^L(x + \hat{\mu}/2) - A_\mu^L(x - \hat{\mu}/2) \right) \equiv \sum_\mu \left(A'_\mu(x) - A'_\mu(x - \hat{\mu}) \right) . \tag{2.22}$$

In momentum space, the lattice Landau gauge condition $\Delta(x) = 0$ reads

$$\sum_\mu q_\mu A_\mu(q) = 0 , \tag{2.23}$$

using the definition of q in Eq. (2.11). It is worth noting that Eq. (2.23) only holds if one defines the gluon field according to Eq. (2.2). If the asymmetric definition A' is used instead, then Eq. (2.23) is replaced by

$$\sum_\mu \left(i \sin \hat{q}_\mu + 1 - \cos \hat{q}_\mu \right) A'_\mu(\hat{q}) = 0 . \tag{2.24}$$

In the limit $a \to 0$ the continuum Landau gauge condition is recovered with $\mathcal{O}(a^2)$ corrections if one uses the field defined in Eq. (2.2) and with $\mathcal{O}(a)$ corrections if A' is used. This makes Eq. (2.2) the preferred definition.

Coming back to the continuum formulation, it is well known that in non-abelian gauge theories, given a typical (regularized) field configuration $A_\mu(x)$, the functional $F_A^c[g]$ will in general have multiple stationary points. These correspond to distinct configurations (Gribov copies), related to each other by gauge transformations, which all satisfy the Landau gauge condition. This is a consequence of the fact that the Faddeev-Popov operator (2.18) is not positive definite. In particular, it can be shown that multiple local minima can occur, so that local minimization of $F_A^c[g]$ does not fix the gauge uniquely. This feature of the theory is preserved on the lattice [15], as it turns out that $F_U^L[g]$ can have multiple stationary points (lattice Gribov copies), and in particular multiple local minima.

Some possible solutions to this problem have been suggested in the literature, mainly aiming to identify the global minimum of the gauge-fixing functional (see for example Ref. [16]). At present, the problem is still open. However, from the point of view of the quantum theory, the relevant issue is to quantify the numerical impact of the residual gauge freedom on gauge-fixed correlation functions. In the framework of a Monte Carlo simulation, one may look for the signature of gauge uncertainty as a "noise" effect, in addition to the purely statistical uncertainty. Previous studies [17,18] indicate that this effect is negligible for most gauge dependent quantities including the gluon propagator.[2] For the purpose of the present investigation we shall therefore assume that for the gluon propagator, the numerical uncertainty associated with Gribov copies effects provides only a small contribution to the overall error bars.

In the continuum formulation of the abelian gauge theory there is no Gribov problem, as the Faddeev-Popov operator reduces to a positive definite, field-independent one. However, it is interesting to notice that abelian Gribov copies may appear on the lattice [19], due to the structure of the lattice Faddeev-Popov operator.

---

[2]The infrared behavior of the ghost propagator may be more sensitive to the removal of Gribov copies [18].

III. SIMULATION PARAMETERS AND METHODS

The details of the simulations are given in Table I. In short, we analyze three lattices, two at $\beta = 6.0$ and one at $\beta = 6.2$, and denote these as the 'large', 'small' and 'fine' lattices respectively. The gauge configurations are generated using a combination of the over-relaxation and Cabibbo–Marinari algorithms. All three lattices are fixed to Landau gauge using a Fourier accelerated steepest descent algorithm [20].

To double-check the gauge fixing we also consider $\sum_{\vec{x}} A_4(\vec{x}, t)$, which should be constant in time when using periodic boundary conditions,

$$\partial_t \sum_{\vec{x}} A_4(\vec{x}, t) = -\sum_{\vec{x}} \partial_i A_i(\vec{x}, t) = 0 \,, \tag{3.1}$$

where we have introduced the shorthand notation

$$\partial_t A_4(\vec{x}, t) \equiv A_4^L(\vec{x}, t + a/2) - A_4^L(\vec{x}, t - a/2) \tag{3.2}$$

$$\partial_i A_i(\vec{x}, t) \equiv A_i^L(\vec{x} + \hat{e}_i/2, t) - A_i^L(\vec{x} - \hat{e}_i/2, t) \tag{3.3}$$

In Fig. 1 we show typical values of $\sum_{\vec{x}} A_4(\vec{x}, t)$ for both the small and the large lattice. As one can see, the time component of the gluon field is constant to 1 part in 10000. Note that the value of one of the color components of the gluon field has no significance in itself, although the fact that it is constant in time has.

IV. FINITE SIZE EFFECTS AND ANISOTROPIES

We begin by considering the effect of the kinematic correction introduced through the change of variables in Eq. (2.11). In the absence of this correction, data in the high momentum region are expected to exhibit significant anisotropy when shown as a function of $\hat{q}$. This is confirmed in Fig. 2, which shows the gluon propagator multiplied by $\hat{q}^2 a^2$ and plotted as a function of $\hat{q}a$. Here and in the following, a Z_3 averaging is performed on the data, where for example the momentum along (x,y,z,t) = (2,1,1,1) is averaged with (1,1,2,1) and (1,2,1,1).

In Fig. 3 the gluon propagator multiplied by $q^2 a^2$ is displayed as a function of qa. We see that the kinematic correction results in a significant reduction in anisotropy in the large momentum region, for $qa > 1.5$. The effect of the kinematic correction is even clearer for the fine lattice, as displayed in Figs 4 and 5. We expect anisotropy arising from finite lattice spacing artefacts to be reduced on this lattice, when the lattice results are compared at the same physical value of q. Rescaling these figures[3] and comparing them at the same physical momenta shows a reduction in the anisotropy compared to the small lattice in both cases. However, this reduction is considerably smaller than the one resulting from applying the kinematic correction on the fine lattice.

---

[3] Recall that the small to fine lattice spacing ratio is $a_s/a_f = 1.4$.

At lower momenta, finite volume effects become significant. These effects are greatest when one or more of the momentum components is zero. Because of the unequal length of the time and spatial axes on our lattices, there is a clear difference not only between on- and off-axis points, but also between the points where three of the components are zero, depending on whether or not one of these lies along the 'long' time axis. In figs. 3 and 5 this is shown by the discrepancy between the filled squares (denoting momenta along one of the spatial axes) and filled triangles (denoting momenta along the time axis).

Fig. 6 displays the gluon propagator data for all momentum directions and values on the large lattice, using the kinematic correction. Again, only a Z_3 averaging has been performed. Examination of the infrared region indicates that finite volume artefacts are very small on the large lattice. In particular, the agreement between purely spatial (filled squares) and time-like momentum vectors (filled triangles) at $qa = 0.20$ appears to indicate that finite size effects are relatively small here.

Some residual anisotropy remains for both the large and small lattices at moderate momenta around $qa \sim 1.5$, despite including the kinematic correction of Eq. (2.11). This anisotropy is clearly displayed in Fig. 3 by the filled squares and triangles denoting momenta directed along lattice axes lying below the majority of points from off-axis momenta for $qa \sim 1.4$. Since tree-level O(4) breaking effects should be removed by the kinematic correction, the remaining anisotropy appears to have its origin in quantum effects beyond tree level. This anisotropy is significantly reduced for the fine lattice, indicating that it is an effect of finite lattice spacing errors as opposed to finite volume errors. The fact that it occurs at the same momentum values and with the same magnitude on both the large and small lattices at $\beta = 6.0$ lends further support to this interpretation.

In order to minimize lattice artefacts for large momentum components we select momentum vectors lying within a cylinder directed along the diagonal $(x, y, z, t) = (1, 1, 1, 1)$ of the lattice. This allows one to access the largest of momenta with the smallest of components. We calculate the distance $\Delta\hat{q}$ of the momentum vector $\hat{q}$ from the diagonal using

$$\Delta\hat{q} = |\hat{q}| \sin\theta_{\hat{q}}, \tag{4.1}$$

where the angle $\theta_{\hat{q}}$ is given by

$$\cos\theta_{\hat{q}} = \frac{\hat{q} \cdot \hat{n}}{|\hat{q}|}, \tag{4.2}$$

and $\hat{n} = \frac{1}{2}(1, 1, 1, 1)$ is the unit vector along the diagonal.

On the small lattice, we found the selection of a cylinder with a radius of one spatial momentum unit ($\Delta\hat{q}a < 1 \times 2\pi/L_s$, where L_s is the number of sites along a spatial axis) provides a reasonable number of points falling along a single curve for large momenta. The data surviving this cut are displayed in Fig. 7. For the large lattice the corresponding physical cut dictates that all momenta must lie within a cylinder of radius two spatial momentum units directed along the lattice diagonal. Fig. 8 displays the data surviving this cut. Fig. 9 shows the data surviving the corresponding cut on the fine lattice, using a radius of 1.5 momentum units, which provides a similar physical radius.

This cut does not address the large finite volume errors surviving in Fig. 7. To remove these problematic momenta, we consider a further cut designed to remove momentum vectors which have one or more vanishing components. This is implemented by keeping only

momentum directions that lie within a certain angle θ_{max} from the diagonal, ie., by keeping $\theta_{\hat{q}} < \theta_{max}$ where $\theta_{\hat{q}}$ is given by Eq. (4.2). We found that a cone of semivertex angle $\theta_{max} = 20°$ was sufficient to provide a set of points lying along a smooth curve. The solid points in Fig. 7 represent these data.

Since finite volume errors on the large lattice are small, it is not necessary to impose the additional cone cut there. However, it is interesting to note that even with this conservative cut, illustrated by the solid points in Fig. 8, the turnover in $q^2 a^2 D(q^2)$ in the infrared region is still observed.

V. RESULTS

A. Tensor structure

Using the Landau gauge condition (2.23), we can infer that the lattice gluon propagator $D^L_{\mu\nu}(q) \equiv \frac{1}{8} \sum_a D^{L,aa}_{\mu\nu}(q)$ should have the following tensor structure, mirroring the continuum form (2.6):

$$D^L_{\mu\nu}(q) = (\delta_{\mu\nu} - \frac{q_\mu q_\nu}{q^2}) D^L(q^2) . \qquad (5.1)$$

By studying the tensor structure of the gluon propagator, we may be able to determine how well the Landau gauge condition is satisfied, and also discover violations of continuum rotational invariance. The tensor structure may be evaluated directly by taking the ratios of different components of $D^L_{\mu\nu}(q)$ for the same value of q. The results for moderate to high momentum values, where we expect Eq. (5.1) to be valid, are summarized in Tables II–IV, and compared to what one would expect from Eq. (5.1), and to what one would obtain by replacing q with $\hat{q}$ in Eq. (5.1). For the small and fine lattices, we have also evaluated the tensor structure using the unfavored asymmetric definition A' of the gluon field.

The selected momentum values in Tables II–IV are not an exhaustive list, but are representative of the respective momentum regimes. It is clear from these tables that our numerical data are consistent with the expectation from Eq. (5.1). In particular, where two of the components of q are zero, this relation is satisfied with a very high degree of accuracy. Where 3 or 4 of the components are non-zero, the errors are larger, but in most cases smaller than 10%. We can also see that in general, the asymmetric definition A' of the gluon field gives results which are inconsistent with this form.

At very low momentum values, we expect finite volume effects to lead to violations of the infinite-volume continuum-limit form (5.1). Tables V–VII show selected ratios of components for the lowest momentum values, displaying, in some cases, significant violations of this form. In particular, the ratio of the $\mu = 4$ (time) component of the diagonal $D^L_{\mu\mu}(q)$ to the other diagonal components is considerably larger than what one would get from Eq. (5.1). The discrepancy is smaller on the large lattice than on the other two lattices, but is still significant at these lowest momenta. This gives us a more rigorous test of finite volume effects than what we could obtain by inspection in Section IV, where finite volume effects were not obvious for the large lattice.

At zero momentum Eq. (5.1) is not well-defined, and the finite volume replacement Eq. (2.8) (with $\xi = 0$) must be used instead. The exact behavior of the functions $h_{\mu\nu}(q)$ and $f(q^2)$ with q and V is not known, but any deviation from $D_{\mu\nu}(q = 0) \propto \delta_{\mu\nu}$ must be due to finite volume effects in $h_{\mu\nu}$ of Eq. (2.8). Table VIII shows the ratios of the diagonal elements for our three lattices. As we can see, the $\mu = 4$ component is in all cases much smaller than the other three components, although the discrepancy is considerably reduced from the small to the large lattice. The small and the fine lattice have a ratio D_{ii}/D_{44} of 3 and 2 respectively, which is equal to the ratio L_t/L_i. For the large lattice, with $L_t/L_i = 2$, $D_{ii}^L/D_{44}^L \approx 1.4$ indicating the reduction of finite volume errors at zero momentum.

B. Asymptotic behavior

The asymptotic behavior of the renormalized gluon propagator in the continuum is given to one-loop level by [5,21]

$$D_R(q^2; \mu) \equiv D_{\text{bare}}(qa)/Z_3(\mu, a) \sim \frac{Z}{q^2} \left(\frac{1}{2} \ln(q^2/\Lambda^2) \right)^{-d_D} , \qquad (5.2)$$

where the constant Z depends on the renormalization scheme and the renormalization point μ, and[4]

$$d_D = \frac{39 - 9\xi - 4N_f}{2(33 - 2N_f)} . \qquad (5.3)$$

In the case we are studying here, both the gauge parameter ξ and the number of fermion flavors N_f are zero, so $d_D = 13/22$.

1. Fits to the asymptotic form

We have fitted the data, with the kinematic correction, for all our three lattices to the asymptotic form in Eq. (5.2) for values of q above ~ 2.7GeV. For the large lattice, we have used the data surviving the cylindrical cut, while for the other two lattices, both the cylindrical and cone cuts have been imposed. Table IX shows the parameter values for the most inclusive of those fits. Other regimes are selected to facilitate comparisons between the three lattices. The largest region providing $\chi^2/N_{df} \simeq 1$ is also indicated.

We see that the asymptotic form fits the data quite well, although the relatively high χ^2 for the fits beginning at $q \sim 2.7$ GeV may be taken as a sign that there are still significant nonperturbative and/or higher loop contributions to the propagator at this momentum scale. The values for the scale parameter Λ are reasonably consistent for the two β-values, although the variation in Λ between different lattices and fit ranges indicates that the one-loop perturbative form is still not valid even at $q^2 = 25$GeV^2.

---

[4]This expression differs by a factor of 2 from the (incorrect) expression given in Ref. [22], which is also quoted in Ref. [9].

2. Matching results for the two lattice spacings

Since the renormalized propagator $D_R(q; \mu)$ is independent of the lattice spacing when the lattice spacing is fine enough (i.e., in the scaling regime), we can use Eq. (2.12) to derive a simple, q-independent expression for the ratio of the unrenormalized lattice gluon propagators at the same physical value of q:

$$\frac{D_f^L(qa_f)}{D_c^L(qa_c)} = \frac{Z_3(\mu, a_f)D_R(q; \mu)/a_f^2}{Z_3(\mu, a_c)D_R(q; \mu)/a_c^2} = \frac{Z_f}{Z_c}\frac{a_c^2}{a_f^2} \tag{5.4}$$

where the subscript f denotes the finer lattice ($\beta = 6.2$ in this study) and the subscript c denotes the coarser lattice ($\beta = 6.0$). We can use this relation to study directly the scaling properties of the lattice gluon propagator by matching the data for the two values of β. This matching can be performed by adjusting the values for the ratios $R_Z = Z_f/Z_c$ and $R_a = a_f/a_c$ until the two sets of data lie on the same curve. It should be emphasized that this procedure matches the lattice data directly, and does not depend on a functional form of the gluon propagator.

In this study, we have used the fine and small lattices to perform this matching, as they have similar physical volumes. The combination of cylindrical and cone cut has been applied to both data sets. We have implemented the matching by making a linear interpolation of the logarithm of the data plotted against the logarithm of the momentum for both data sets. In this way the scaling of the momentum is accounted for by shifting the fine lattice data to the right by an amount Δ_a as follows

$$\ln D_c^L(\ln(qa_c)) = \ln D_f^L(\ln(qa_c) - \Delta_a) + \Delta_Z \tag{5.5}$$

Here Δ_Z is the amount by which the fine lattice data must be shifted up to provide the optimal overlap between the two data sets. The matching of the two data sets has been performed for values of Δ_a separated by a step size of 0.001. Δ_Z is determined for each value of Δ_a considered, and the optimal combination of shifts is identified by searching for the global minimum of χ^2/N_{df}. The ratios R_a and R_Z are related to Δ_a and Δ_Z by

$$R_a = e^{-\Delta_a}, \qquad R_Z = R_a^2 e^{-\Delta_Z} . \tag{5.6}$$

Figure 10 shows the data for both lattice spacings as a function of qa before shifting. In Fig. 11 we present the result of the matching using $\hat{q}$ as the momentum variable. The minimum value for χ^2/N_{df} of about 1.7 is obtained for $R_a \sim 0.815$. This value for R_a is considerably higher than the value of 0.716 ± 0.040 obtained from an analysis of the static quark potential in Ref. [23]. From this discrepancy, as well as the relatively high value for χ^2/N_{df}, we may conclude that the gluon propagator, taken as a function of $\hat{q}$, does not exhibit scaling behavior for the values of β considered here.

Fig. 12 shows the result of the matching using q as the momentum variable. We can see immediately that this gives much more satisfactory values both for χ^2/N_{df} and for R_a. The minimum value for χ^2/N_{df} of 0.6 is obtained for $R_a = 0.745$. Taking a confidence interval where $\chi^2/N_{df} < \chi^2_{\min} + 1$ gives us an estimate of $R_a = 0.745^{+32}_{-37}$, where the errors denote the uncertainty in the last digits. This is fully compatible with the value of 0.716 ± 0.040

obtained from Ref. [23]. The corresponding estimate for the ratio of the renormalization constants is $R_Z = 1.038^{+26}_{-21}$. That $R_Z \geq 1$ is consistent with what one would expect from continuum perturbation theory.

<h3 style="text-align:center">C. Model functions</h3>

Having verified scaling in our lattice data over the entire range of q^2 considered, we will now proceed with model fits. We have considered a number of functional forms, based on a variety of theoretical suggestions from the literature. All these forms, as well as the new models we have constructed in this study, include an overall dimensionless renormalization parameter Z. This parameter is not equal to the renormalization constant Z_3, although the two can be related for each individual model.

We introduce an infrared-regulated version $L(q^2, M)$ of the one-loop logarithmic correction given by Eq. (5.2) in order to ensure that these models have the correct leading ultraviolet behavior. This is given by

$$L(q^2, M) \equiv \left[\frac{1}{2} \ln \left((q^2 + M^2)(q^{-2} + M^{-2}) \right) \right]^{-d_D} . \tag{5.7}$$

The factor $q^{-2} + M^{-2}$ ensures that $L(q^2, M)$ is properly regulated in the infrared.

For simplicity of presentation of the models, all model formulae are to be understood as functions of dimensionless quantities (scaled by the appropriate powers of the lattice spacing a). The models considered here are:

Gribov [1]

$$D^L(q^2) = \frac{Zq^2}{q^4 + M^4} L(q^2, M) \tag{5.8}$$

Stingl [2]

$$D^L(q^2) = \frac{Zq^2}{q^4 + 2A^2q^2 + M^4} L(q^2, M) \tag{5.9}$$

Marenzoni [12]

$$D^L(q^2) = \frac{Z}{(q^2)^{1+\alpha} + M^2} \tag{5.10}$$

Cornwall I [8]

$$D^L(q^2) = Z \left[(q^2 + M^2(q^2)) \ln \frac{q^2 + 4M^2(q^2)}{\Lambda^2} \right]^{-1} \tag{5.11}$$

where

$$M(q^2) = M \left\{ \frac{\ln \frac{q^2 + 4M^2}{\Lambda^2}}{\ln \frac{4M^2}{\Lambda^2}} \right\}^{-6/11}$$

Cornwall II [24]

$$D^L(q^2) = Z\left[(q^2 + M^2))\ln\frac{q^2 + 4M^2}{\Lambda^2}\right]^{-1} \quad (5.12)$$

Cornwall III [24]

$$D^L(q^2) = \frac{Z}{q^2 + Aq^2\ln(q^2/M^2) + M^2} \quad (5.13)$$

Here, Z, M, A, Λ and α are parameters to be optimized in the fit. In addition, we study the following 4-parameter forms:

Model A:

$$D^L(q^2) = Z\left[\frac{AM^{2\alpha}}{(q^2 + M^2)^{1+\alpha}} + \frac{1}{q^2 + M^2}L(q^2, M)\right] \quad (5.14)$$

Model B:

$$D^L(q^2) = Z\left[\frac{AM^{2\alpha}}{(q^2)^{1+\alpha} + (M^2)^{1+\alpha}} + \frac{1}{q^2 + M^2}L(q^2, M)\right] \quad (5.15)$$

Model C:

$$D^L(q^2) = Z\left[\frac{A}{M^2}e^{-(q^2/M^2)^\alpha} + \frac{1}{q^2 + M^2}L(q^2, M)\right] \quad (5.16)$$

We have also considered special cases of the three forms (5.14)–(5.16), with specific values for the exponent α. All these models are constructed to exhibit the asymptotic behavior of Eq. (5.2).

<div align="center">

D. Numerical results

</div>

The fits are performed to the large lattice data using the cylindrical cut, and excluding the first point (at $qa \sim 0.1$), which may be sensitive to the volume of the lattice. To balance the sensitivity of the fit over the available range of qa, we have averaged adjacent lattice momenta lying within $\Delta qa < 0.005$.

In order to determine the stability of the fits, we have varied the starting point and width of the fit. After averaging over adjacent momenta, the data points are numbered 1,2,...,142. The starting point has been incremented in steps of 2, and for each starting point the width has been varied in steps of 2 between the minimum possible width (ie, the number of parameters plus 1) and the maximum width. The statistical uncertainty in the parameters is determined using a jackknife procedure [25]. Since the number of points in most of the fits is larger than the number of configurations, we have not been able to compute χ^2 using the full covariance matrix [26]. However, in the cases where this is possible, the results are compatible with those achieved using the 'naïve' χ^2.

Table X shows the values for χ^2/N_{df} for each of the models (5.8)–(5.13). Unfortunately, none of these models succeed in providing an acceptable fit over the entire available momentum range. In the case of Marenzoni's model (5.10), this is not surprising, since this model does not have the correct asymptotic behavior. Our models, Model A and Model B, are constructed as generalizations of Eq. (5.10) which should remedy this problem. Of the models put forward in the literature, we note that Cornwall's proposal (5.11) lies closest to the data.

Fig. 13 shows χ^2/N_{df} as functions of the starting point and width (in number of points) of the fits, for fits to Models A–C. Of these three, only Model A is able to account properly for the infrared behavior of the gluon propagator, while Models B and C yield values for χ^2/N_{df} of 14 and 12 respectively. All the models give reasonable fits to the data for intermediate momentum ranges.

Fit parameters for Model A are illustrated in Fig. 14. All the parameters, in particular M and α, are well determined and stable over the most interesting regions (fits with a large number of points, including the infrared). In the ultraviolet region alone, all the parameter values become unstable. This is expected, since we found in Section V B that a 2-parameter form is sufficient to describe the data in this region. There the 4-parameter forms, Models A–C, will be poorly constrained.

Figs. 15 and 16 show the best fit of Model A. We see that this provides a near perfect fit to the data. The optimal fit parameters are shown in Table XI. Fig. 17 shows fits of several other models, which we can see fail to account properly for the data.

Table XI also shows the parameter values for Marenzoni *et al*'s model (5.10) and Cornwall's model (5.11). The values quoted are for fits to all the available data, while the errors denote the spread in parameter values resulting from varying the fitting range. The statistical errors are in all cases much smaller than the systematic errors associated with varying the fit regime. In the case of Model C, the variation in parameter values becomes unstable in the usual fitting ranges; in order to avoid this problem, we have chosen a more restricted set of fitting ranges to evaluate the uncertainties than for the other models.

In order to determine the dependence of our models on the exact functional form used to regulate the ultraviolet term in the infrared, we have performed fits to Eqs. (5.14) and (5.15) (Models A and B) with $L(q^2, M) \to L(q^2, \sqrt{2}M)$ and with $L(q^2, M) \to L(q^2, M/\sqrt{2})$, altering the relationship between masses in the infrared and ultraviolet terms. This turns out to have a significant effect both on χ^2/N_{df} and on the values for the fit parameters. The quality of the fit deteriorates substantially as $M \to \sqrt{2}M$ in the logarithm, while it improves slightly as $M \to M/\sqrt{2}$. The value for the exponent α changes by more than 2σ, and this feeds through to the other parameters, although the value for M remains approximately within 1σ of its original value. The relative performance of Model A and Model B is not affected, and Model A remains clearly the preferred model of these two.

VI. DISCUSSION AND CONCLUSIONS

14

A. Comparison of different models

We find that none of the models from the literature give a satisfactory fit to the data. It can be argued that Stingl's form (5.9) is only supposed to be valid in the deep infrared. We do not have sufficient data in this region, or control over the volume dependence of the data at our lowest momentum values, to be able to distinguish between the performance of the various models in this region alone (i.e., the first 10 points in our fits). All models give a reasonable χ^2/N_{df} when we fit to only the first 10–20 points. A generalisation of Stingl's form has been used to fit to lattice data at high momentum values [27], but these results are not directly comparable to ours, since they are obtained for a different choice of gauge and do not include the infrared region ($\hat{q}_{\min} = 1$ GeV). In the case of Cornwall's proposal (5.11) it should also be mentioned that this form was derived using a gauge-invariant 'pinch technique', and may not be directly comparable to our Landau gauge results.

We have found that the data can be adequately described by two terms: one governing the ultraviolet behavior according to the one-loop perturbative formula, and the other providing the infrared behavior. The infrared term is proportional to $(q^2+M^2)^{-\alpha}$ with $\alpha \approx 3$. It should be emphasized at this point that the performance of Model A, and in particular the value of the exponent α, depends substantially on the exact form chosen for the logarithmic function $L(q^2, M)$ in order to regulate the ultraviolet term in the infrared. Given a particular form for D_{UV}, all the parameter values are very stable and lend credence to Model A as correctly encapsulating the lattice results. It should be noted, however, that although the 1-loop perturbative form does provide an adequate fit in the ultraviolet, we found in Sec. V B 1 that the parameter values are not stable. The 2-loop form should be an improvement on this. The third model we considered, using an exponential function rather than a 'mass' term to describe the infrared behavior, was clearly unsatisfactory.

Our approach here differs significantly from those of previous studies [11,12]. Firstly, in order to reduce the effect of lattice artefacts at high momenta, we use the momentum variable q defined in Eq. (2.11) rather than the 'naive' momentum variable $\hat{q}$. We believe this approach has been justified by the verification of scaling in Section V B. A similar approach has been used in a recent study of the three-gluon vertex [28]. Furthermore, we select an improved and larger set of momenta to the ones used in those previous studies. With this in mind, it should nevertheless be possible to make at least an approximate comparison between the results at small to intermediate momenta.

Both previous studies [11,12] fit their data to Marenzoni's form (5.10) or special cases of this model (with $M = 0$ or $\alpha = 0$), which we have found does not account satisfactorily for the data. In addition, in Ref. [11] the low-momentum data are fitted to the Gribov form (5.8). The latter form fails to provide us with any fit which would make a comparison of parameter values meaningful. However, we may compare the values we obtain for the parameter α in the Marenzoni form of Eq. (5.10) with those of Refs. [11,12]. Although χ^2/N_{df} for fits to all the data with this model is very high, the value for α is reasonably stable over a large region, including fits where $\chi^2/N_{df} \sim 1$. We find $\alpha \sim 0.3$, in agreement with the value quoted in Ref. [11]. This is inconsistent with the value of ~ 0.5 quoted in Ref. [12]. However, this value is obtained by fitting only to data in the infrared region. If we restrict ourselves to the same region, we also obtain a value of $\alpha \sim 0.5$. Hence, when repeating the analysis of Refs. [11,12], we find results consistent with theirs.

15

We find that Model A provides a fit to the data throughout the entire available momentum range. However, we are unaware of any current physical interpretation of this model, in contrast to the models arising from the approximate analytical studies by Gribov, Stingl and Cornwall [1,2,8].

B. Finite volume effects

The asymmetry of the lattices, with $L_t = 3L_s$ for the small lattice and $L_t = 2Ls$ for the large and fine lattices, is one of the measures used to assess finite volume effects. By comparing momenta along the time axis with momenta along the spatial axes, we find that finite volume errors are small on the large lattice, even at low momentum values. A 'cone' cut along the diagonal in momentum space is imposed for the smaller lattices to remove finite volume effects, but this cut is not found to be necessary for the large lattice.

Inspection of the tensor structure reveals some residual finite volume effects in the order of 10–15% at the lowest momentum values. Apart from these 4–6 points, finite volume effects are negligible. Excluding these points does not change the parameter values. Nor will the relative performance of our models be affected. Implementing the 'cone' cut on the large lattice will have a similar effect to excluding these points.

Comparing the data at low momenta for the two lattices at $\beta = 6.0$, we find that the value of the gluon propagator decreases with increasing volume. This opens up the possibility that in the infinite-volume limit, the propagator may be strongly suppressed or even vanishing at extremely small momenta, as suggested by Gribov and Stingl [1,2]. Recent studies at strong coupling and in lower dimensions [29–31] lend some support to this possibility.

C. Finite lattice spacing effects

The kinematic correction $\hat{q} \rightarrow q$ gives a large reduction in finite lattice spacing anisotropy at high momentum values, but does not remove this anisotropy completely. A 'cylinder' cut along the diagonal in momentum space is imposed on all lattices to remove this residual anisotropy.

We have verified scaling of the gluon propagator for momenta $q > 1.3$ GeV between $\beta = 6.0$ and $\beta = 6.2$. This scaling is dependent on the kinematic correction $\hat{q} \rightarrow q$. If $\hat{q}$ is used as the momentum variable, scaling fails, even after the 'cylinder' and 'cone' cuts are imposed. We are currently working on using improved actions [32,33] to reduce or remove finite lattice spacing effects.

D. Conclusion

We have calculated the gluon propagator on a large volume lattice and verified that finite volume effects are under control. Finite volume effects in the order of 10% are found for the very lowest momentum values, but become insignificant for $q > 600$ MeV. Finite lattice spacing effects are handled by using the kinematic correction $\hat{q}_\mu \rightarrow q_\mu = (2/a)\sin(\hat{q}_\mu a/2)$,

and by selecting momenta along the 4-dimensional diagonal. Scaling is verified between $\beta = 6.0$ and 6.2.

The propagator is found to be well represented by the functional form $D(q^2) = D_{\mathrm{IR}} + D_{\mathrm{UV}}$, where $D_{\mathrm{IR}} = AM^{2\alpha}(q^2 + M^2)^{-(1+\alpha)}$ and D_{UV} is an infrared regulated version (see Eqs. (5.7) and (5.14)) of the one-loop asymptotic form defined in Eq. (5.2). Our best estimate for the parameter α is $\alpha = 2.2^{+0.1+0.2}_{-0.2-0.3}$, where the second set of errors represents the systematic uncertainty arising from the choice of infrared regulator for D_{UV}. Using the regulator given in Eq. (5.7), our best estimates for the parameters M and A are $M = (1020 \pm 100 \pm 25)$ MeV and $A = 9.8^{+0.1}_{-0.9}$, where the second set of errors in M represents the statistical uncertainty in the lattice spacing quoted in Table I.

Among the issues still under consideration are an extrapolation of $D(q^2)$ to infinite volume at low q^2, as well as an evaluation of the effect of Gribov copies and of the gauge dependence of the gluon propagator. Work is also in progress to calculate the gluon propagator using improved actions, thereby reducing finite lattice spacing effects and allowing simulations on larger physical volumes.

ACKNOWLEDGMENTS

REFERENCES

[1] V.N. Gribov, *Nucl. Phys.* **B 139**, 19 (1978); D. Zwanziger, *Nucl. Phys.* **B 378**, 525 (1992)

[2] M. Stingl, *Phys. Rev.* **D 34**, 3863 (1986); *Phys. Rev.* **D 36**, 651 (1987); U. Häbel et al, *Z. Phys.* **A 336**, 423 (1990)

[3] L. von Smekal, A. Hauck, R. Alkofer, *Phys. Rev. Lett.* **79**, 3591 (1997) (hep-ph/9705242)l *Ann. Phys.* **267**, 1 (1998) (hep-ph/9707327)

[4] D. Atkinson and J.C.R. Bloch, hep-ph/9712459 and *Mod. Phys. Lett* **A 13**, 1055 (1998) (hep-ph/9802239)

[5] S. Mandelstam, *Phys. Rev.* **D 20**, 3223 (1979)

[6] M. Baker, J.S. Ball, F. Zachariassen, *Nucl. Phys.* **B 186**, 531 (1981)

[7] N. Brown and M.R. Pennington, *Phys. Rev.* **D 39**, 2723 (1989)

[8] J. Cornwall, *Phys. Rev.* **D 26**, 1453 (1982)

[9] C.D. Roberts and A.G. Williams, *Progress in Particle and Nuclear Physics* **33**, 477–575 (1994)

[10] F.T. Hawes, P. Maris and C.D. Roberts, nucl-th/9807056

[11] C. Bernard, C. Parrinello, A. Soni, *Phys. Rev.* **D49**, 1585 (1994) (hep-lat/9307001)

[12] P. Marenzoni, G. Martinelli, N. Stella, *Nucl. Phys.* **B 455**, 339 (1995) (hep-lat/9410011); P. Marenzoni, G. Martinelli, N. Stella, M. Testa, *Phys. Lett.* **B 318**, 511 (1993)

[13] D.B. Leinweber, J.I. Skullerud, A.G. Williams, C. Parrinello, *Phys. Rev.* **D 58**, 031501 (1998) (hep-lat/9803015)

[14] A. Cucchieri and T. Mendes, *Nucl. Phys.* **B 471**, 263 (1996) (hep-lat/9511020)

[15] E. Marinari, C. Parrinello, R. Ricci, *Nucl. Phys.* **B 362**, 487 (1991)

[16] J. Hetrick and Ph. de Forcrand, *Nucl. Phys.* **B (Proc. Suppl.) 63**, 838 (1998) (hep-lat/9710003)

[17] M.L. Paciello et al, *Phys. Lett.* **B 341**, 187 (1994)

[18] A. Cucchieri, *Nucl. Phys.* **B 508**, 353 (1997) (hep-lat/9705005)

[19] P. de Forcrand, J. E. Hetrick, A. Nakamura, and M. Plewnia, *Nucl. Phys.* **B (Proc. Suppl.) 20**, 194 (1991)

[20] C.T.H. Davies et al, *Phys. Rev.* **D 37**, 1581 (1988)

[21] G. dell'Antonio and D. Zwanziger, *Nucl. Phys.* **B 326**, 333 (1989)

[22] W. Marciano and H. Pagels, *Phys. Rep.* **36**, 137 (1977)

[23] G.S. Bali and K. Schilling, *Phys. Rev.* **D 47**, 661 (1993)

[24] J. Cornwall, private communication

[25] B. Efron, *Society for Industrial and Applied Mathematics Review* **21**, 460 (1979)

[26] C. Michael, *Phys. Rev.* **D 49**, 2616 (1994) (hep-lat/9310026)

[27] H. Aiso et al, *Nucl. Phys.* **B (Proc. Suppl.) 53**, 570 (1997)

[28] Ph. Boucaud et al, *JHEP* **10**, 017 (1998) (hep-ph/9810322)

[29] H. Nakajima and S. Furui, hep-lat/9809081

[30] A. Cucchieri, *Phys. Lett.* **B 422**, 233 (1998) (hep-lat/9709015)

[31] A. Cucchieri, hep-lat/9810022

[32] K. Symanzik, *Nucl. Phys.* **B 226**, 187 (1983); M. Alford et al, *Phys. Lett.* **B 361**, 87 (1995) (hep-lat/9507010)

[33] F.D.R. Bonnet et al, hep-lat/9905006
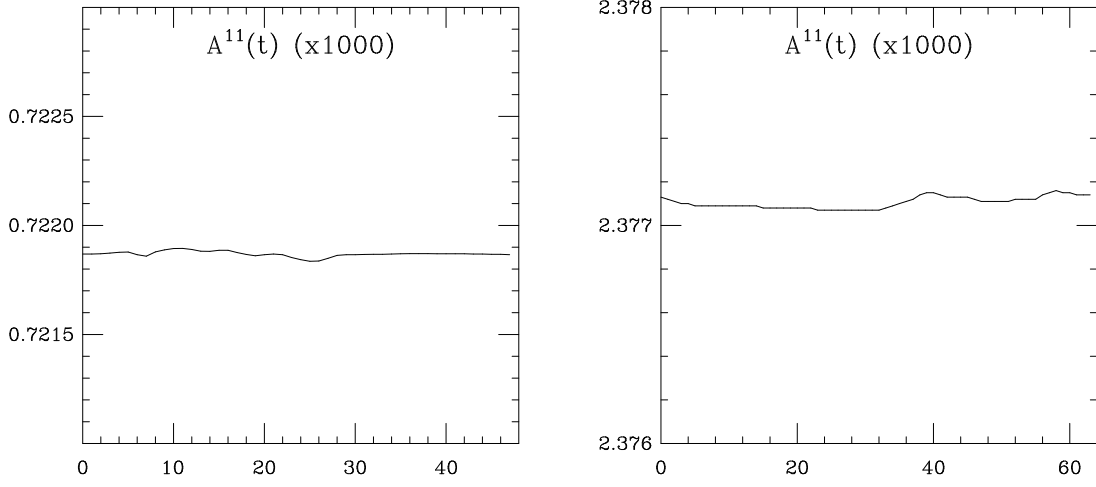
FIGURES

FIG. 1. Plots of the (1,1) color component of $\sum_{\vec{x}} A_4(\vec{x}, t)$ as a function of t for one gauge fixed configuration on the small lattice (left), and on the large lattice (right).
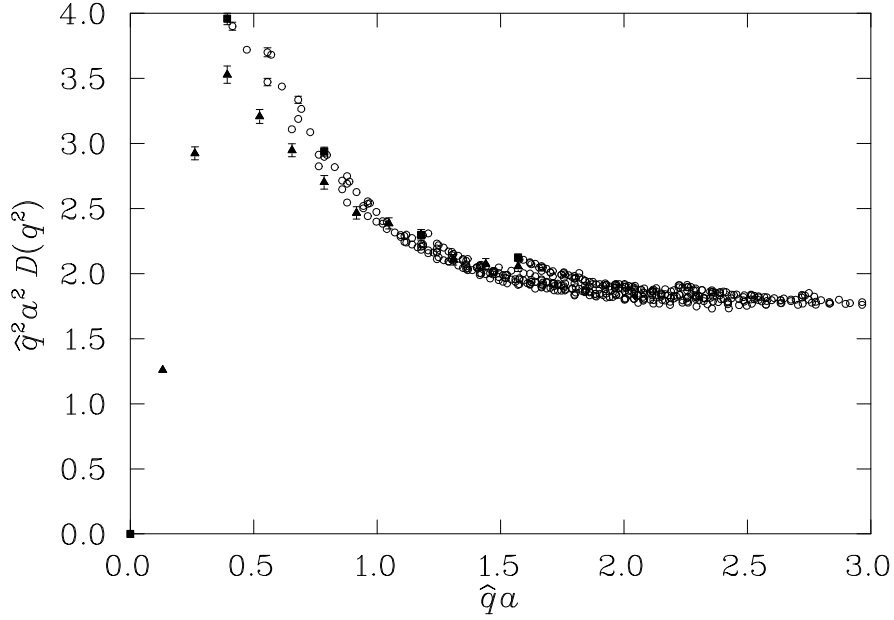

FIG. 2. The gluon propagator from the small lattice multiplied by $\hat{q}^2 a^2$ plotted as a function of momenta $\hat{q}a$. Values for each momentum direction are plotted separately. Only a Z_3 averaging has been performed. Filled squares denote momenta directed along spatial axes, while filled triangles denote momenta directed along the time axis. Other momenta are indicated by open circles.
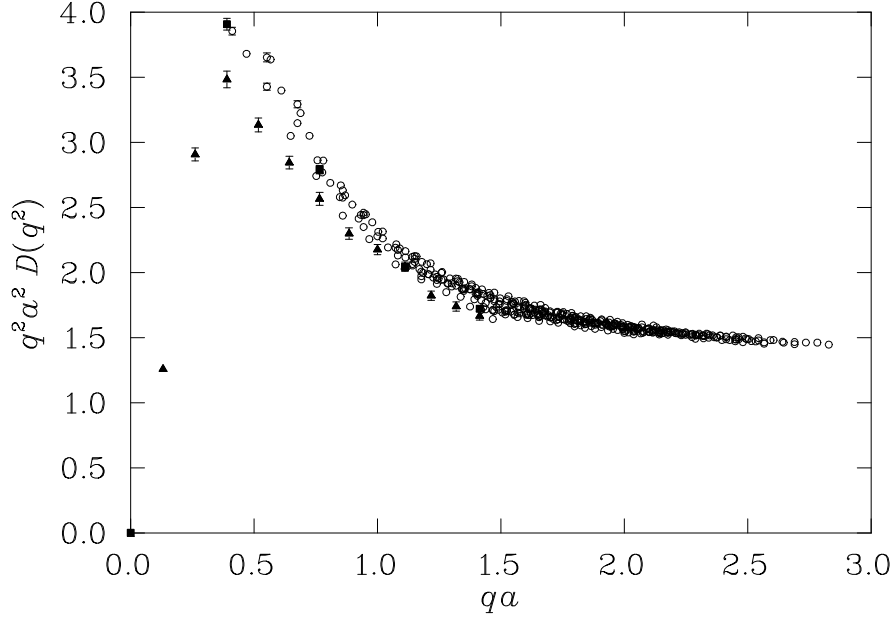
20

FIG. 3. The gluon propagator from the small lattice multiplied by q^2a^2 plotted as a function of momenta qa. The symbols are as in Fig. 2.
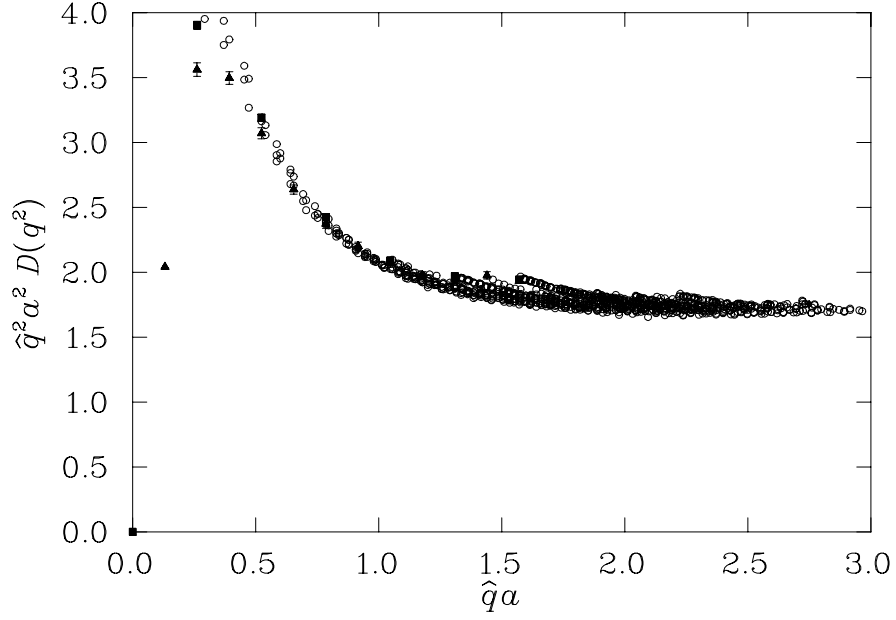

FIG. 4. The gluon propagator from the fine lattice multiplied by $\hat{q}^2a^2$ plotted as a function of momenta $\hat{q}a$. The symbols are as in Fig. 2.
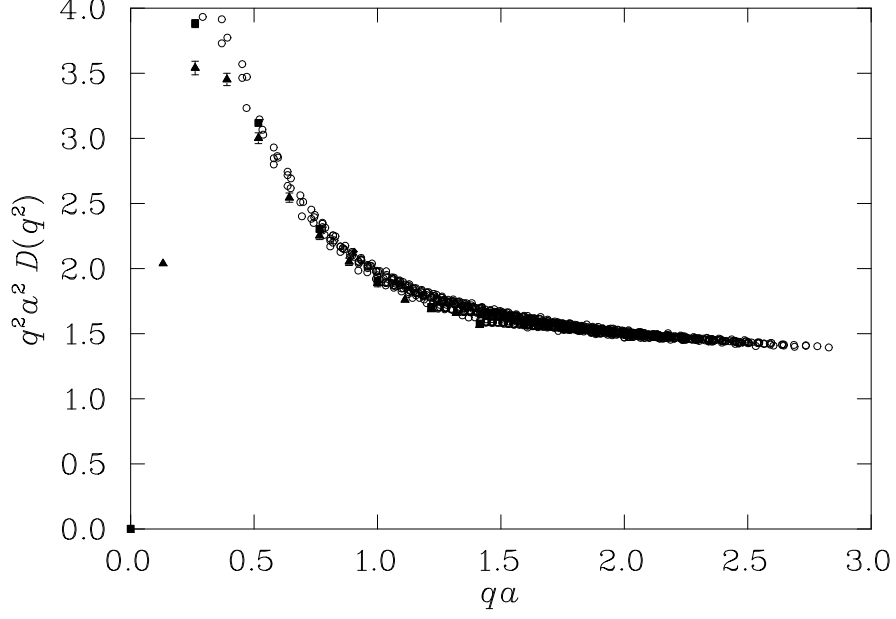
FIG. 5. The gluon propagator from the fine lattice multiplied by $q^2 a^2$ plotted as a function of momenta qa. The symbols are as in Fig. 2.
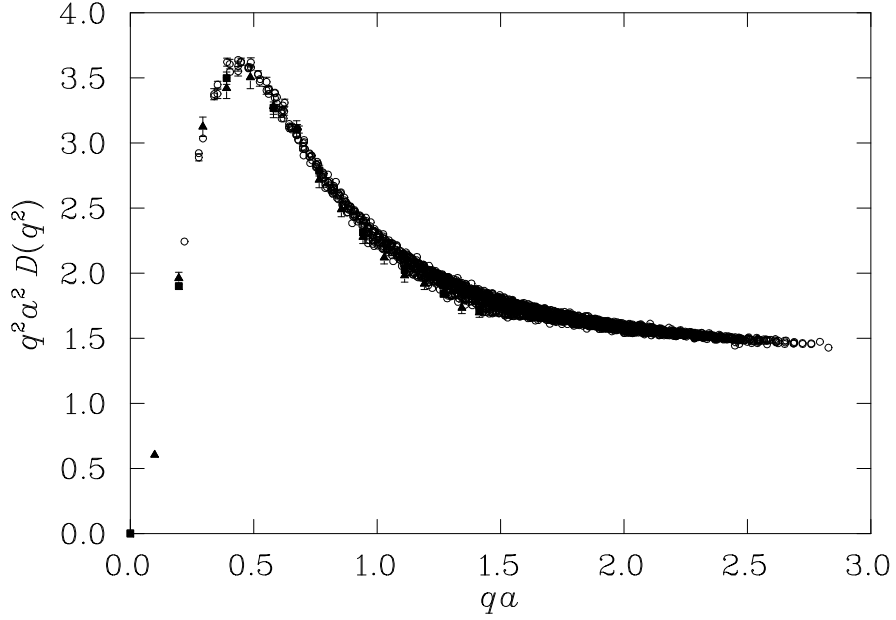
FIG. 6. The gluon propagator from the large lattice multiplied by $q^2 a^2$ plotted as a function of momenta qa. Values for each momentum direction are plotted separately. Only a Z_3 averaging has been performed for the data shown in this figure. Plotting symbols are as in Fig. 2. Finite volume errors are greatly reduced compared to the results from the smaller lattice, as displayed by the overlap of points obtained from spatial and time-like momentum vectors. However, significant anisotropy is apparent for larger momenta.

FIG. 7. The gluon propagator from the small lattice multiplied by $q^2 a^2$. The points displayed in this plot lie within a cylinder of radius $\Delta \hat{q} a < 1 \times 2\pi/16$ directed along the diagonal $(x, y, z, t) = (1, 1, 1, 1)$ of the lattice. The solid points also lie within a cone of $20°$ measured from the diagonal at the origin.
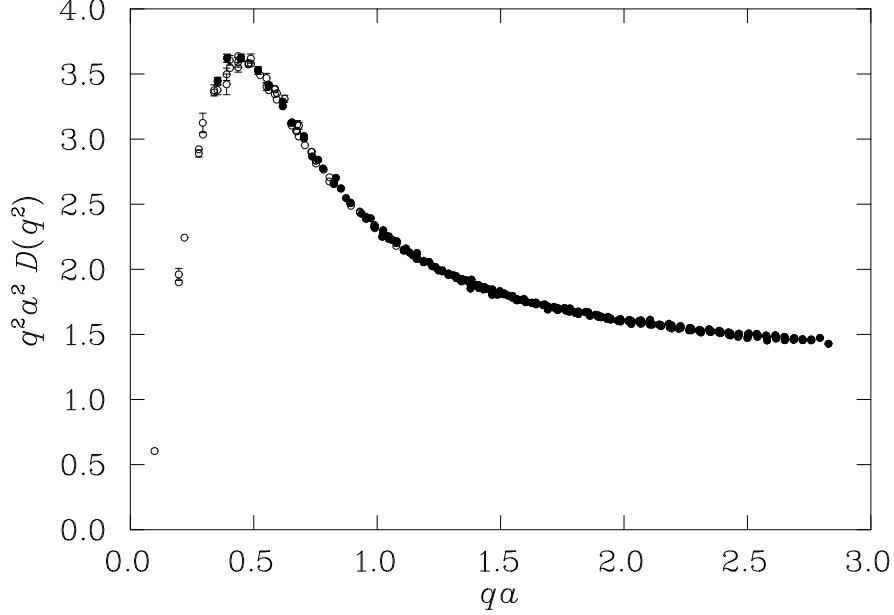
FIG. 8. The gluon propagator from the large lattice multiplied by $q^2 a^2$. The points displayed in this plot lie within a cylinder of radius $\Delta \hat{q} a < 2 \times 2\pi/32$ directed along the diagonal of the lattice. The solid points also lie within a cone of $20°$ measured from the diagonal at the origin.
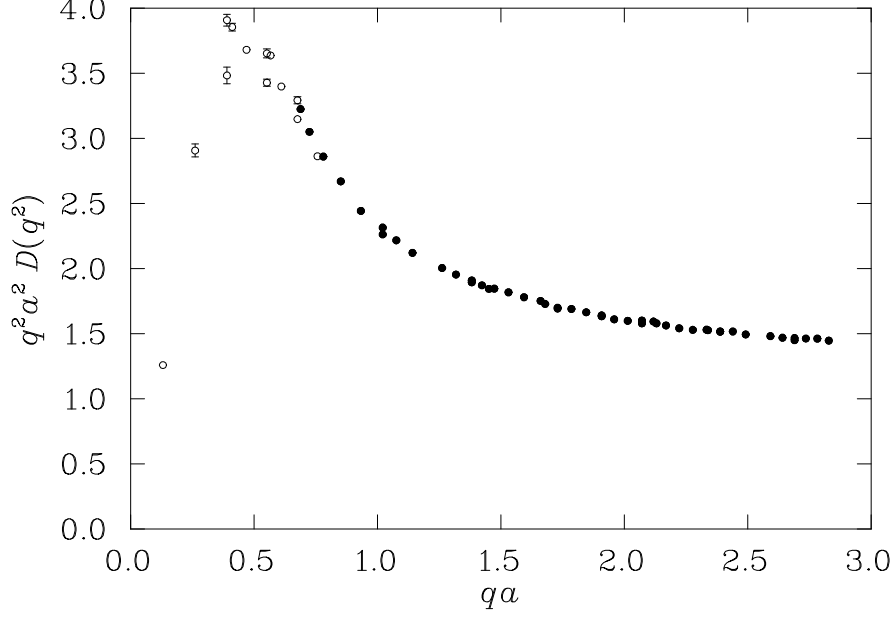
23
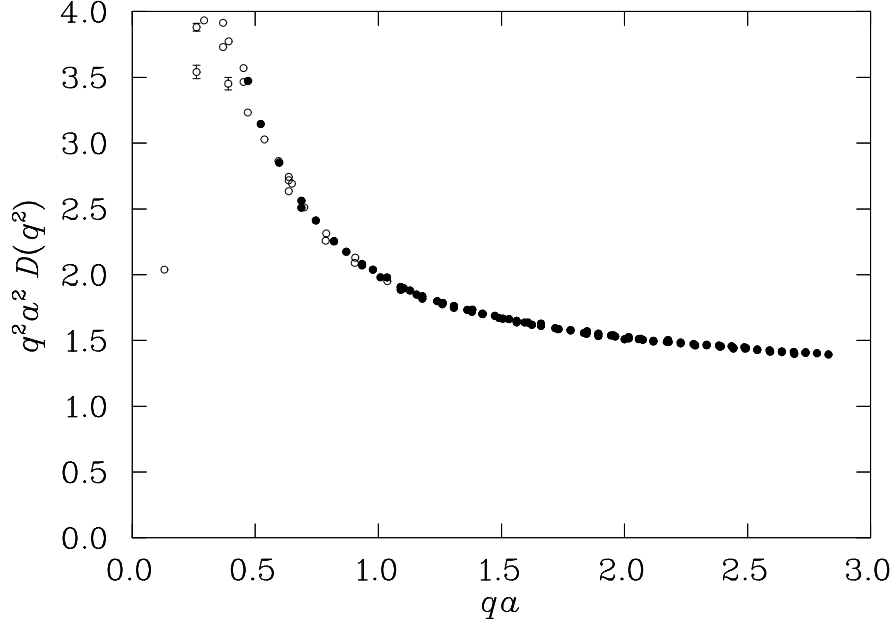
FIG. 9. The gluon propagator from the fine lattice multiplied by q^2a^2. The points displayed in this plot lie within a cylinder of radius $\Delta \hat{q} a < 1.5 \times 2\pi/32$ directed along the diagonal of the lattice. The solid points also lie within a cone of 20° measured from the diagonal at the origin.
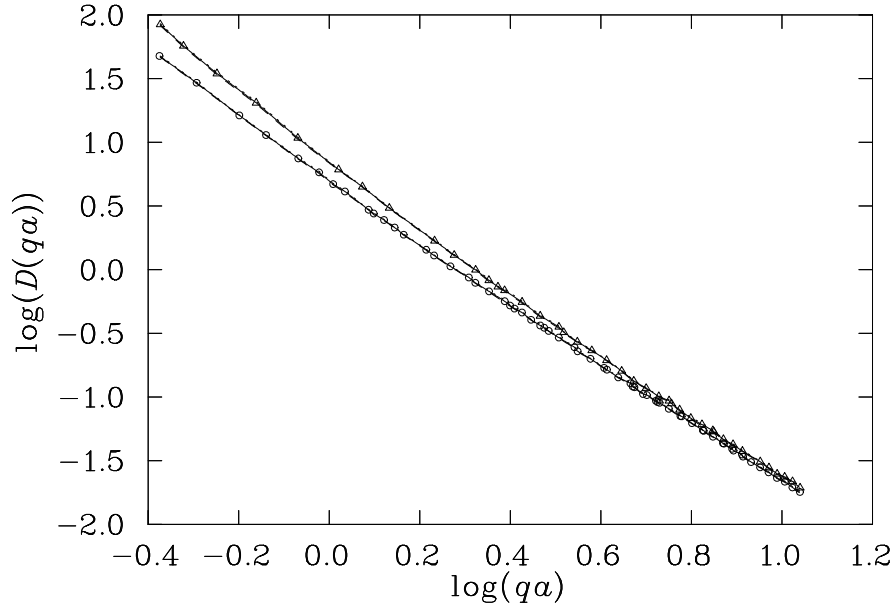
FIG. 10. The dimensionless, unrenormalized gluon propagator as a function of $\ln(qa)$ for the two values of β. The triangles denote the data for the small (coarse) lattice at $\beta = 6.0$, while the circles denote the data for $\beta = 6.2$. The lines represent linear interpolations between the data points.
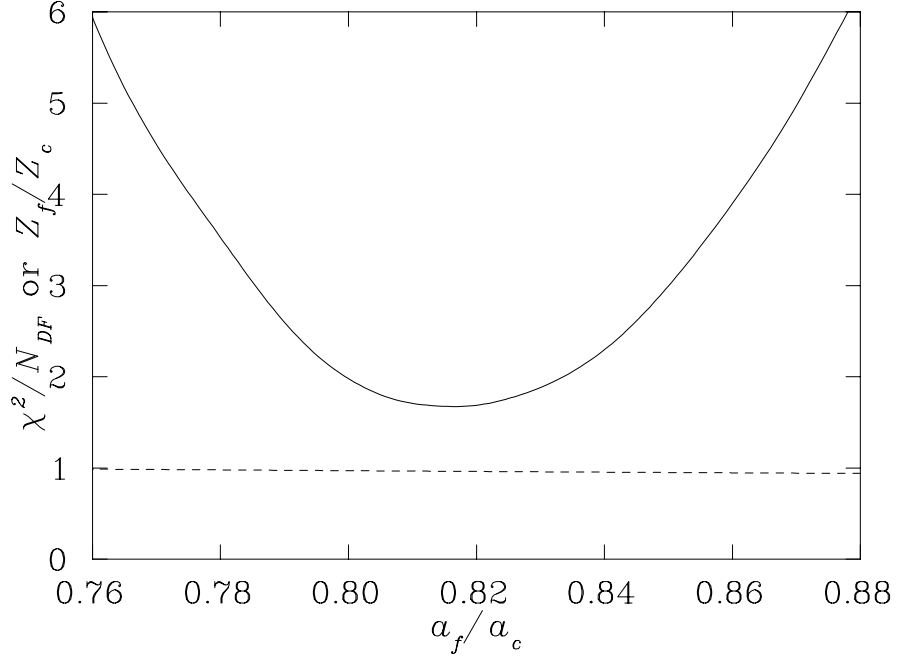
FIG. 11. χ^2 per degree of freedom as a function of the ratio of lattice spacings for matching the small and fine lattice data, using $\hat{q}$ as the momentum variable. The dashed line indicates the ratio R_Z of the renormalization constants.
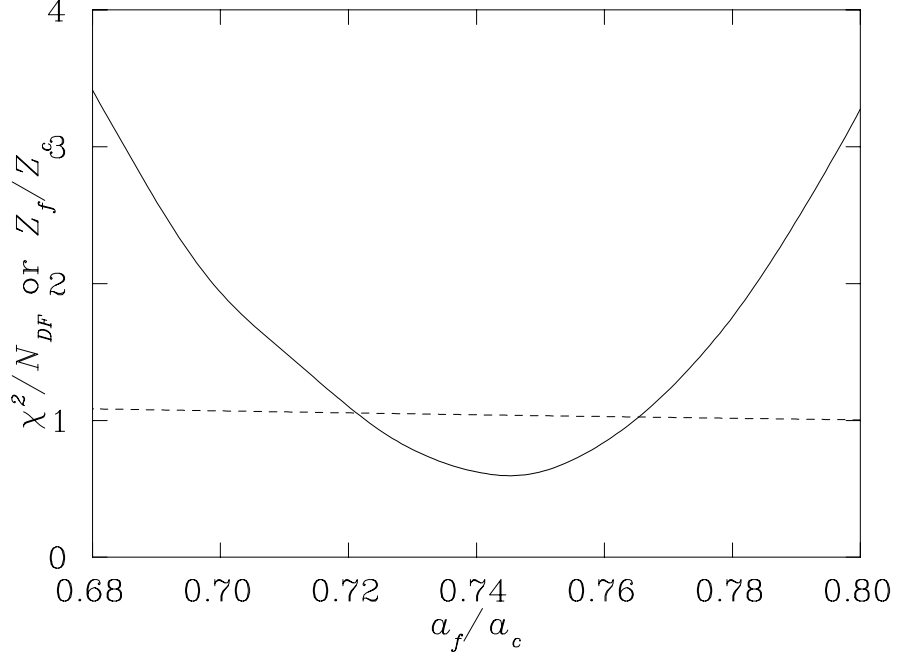
FIG. 12. χ^2 per degree of freedom as a function of the ratio of lattice spacings for matching the small and fine lattice data, using q as the momentum variable.
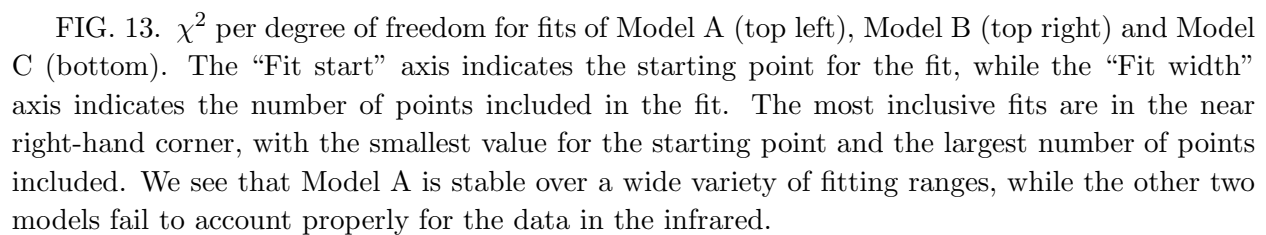
FIG. 13. χ^2 per degree of freedom for fits of Model A (top left), Model B (top right) and Model C (bottom). The "Fit start" axis indicates the starting point for the fit, while the "Fit width" axis indicates the number of points included in the fit. The most inclusive fits are in the near right-hand corner, with the smallest value for the starting point and the largest number of points included. We see that Model A is stable over a wide variety of fitting ranges, while the other two models fail to account properly for the data in the infrared.

FIG. 14. Stability plots for Model A. All the parameter values are stable over the region of interest.
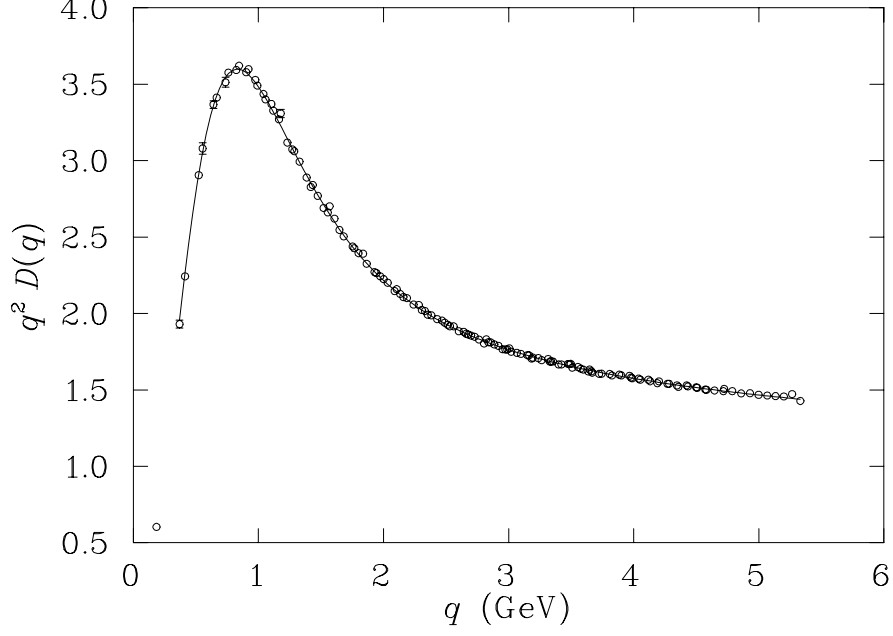
FIG. 15. The gluon propagator multiplied by q^2, with nearby points averaged. The line illustrates our best fit of Model A defined in (5.14). The fit is performed over all points shown, excluding the one at the lowest momentum value, which may be sensitive to the finite volume of the lattice. The scale is taken from the value for the string tension quoted in Ref. [23].
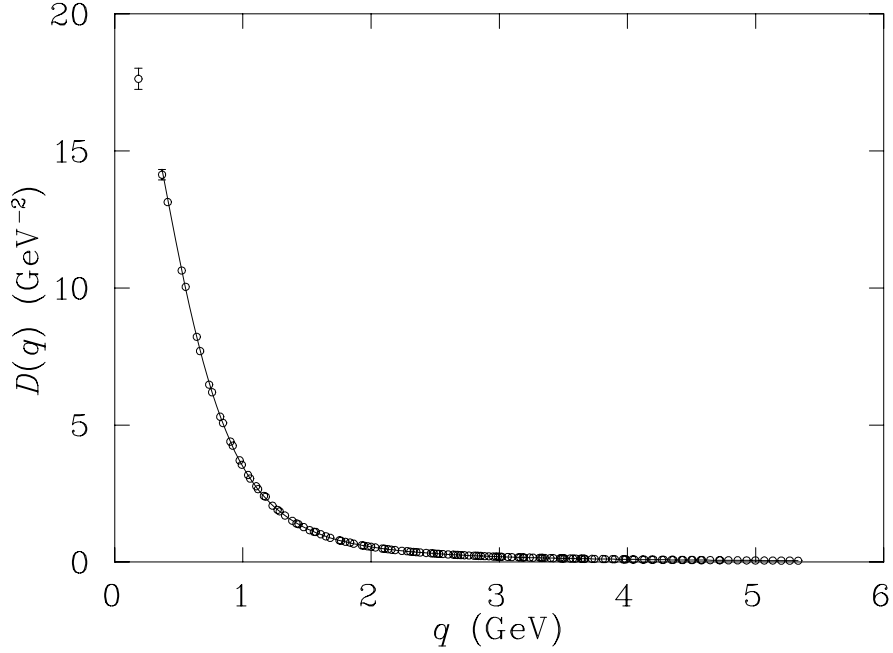
FIG. 16. The gluon propagator in physical units. The line illustrates our best fit of Model A, as in Fig. 15.
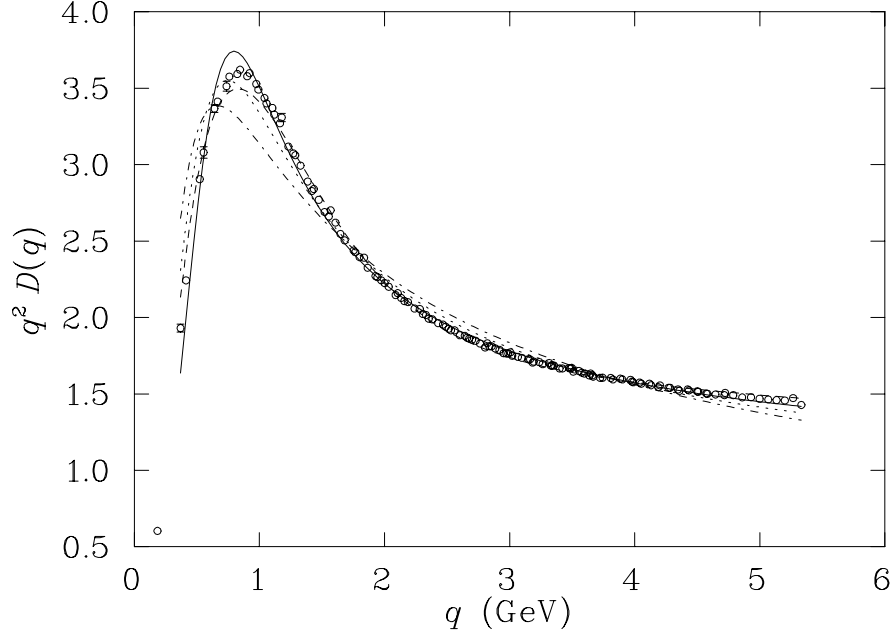
FIG. 17. The gluon propagator multiplied by q^2, with nearby points averaged. The lines illustrate the best fit of various other models. The solid line is Model B, the dotted line is Cornwall I, the dash-dotted line is Marenzoni and the dashed line is Model C.

TABLES

Name	β	$a\sqrt{K}$	a^{-1} (GeV)	Volume	N_{config}	Separation	θ_{max}	$\langle U \rangle$
Small	6.0	0.2265(55)	1.885(45)	$16^3 \times 48$	125	800	10^{-12}	0.860939(31)
Large	6.0	0.2265(55)	1.885(45)	$32^3 \times 64$	75	1000	10^{-12}	0.861793(15)
Fine	6.2	0.1619(19)	2.637(30)	$24^3 \times 48$	223	2400	10^{-12}	0.873948(15)

TABLE I. Simulation parameters. The values for the string tension $a\sqrt{K}$ are taken from Ref. [23], and the lattice spacings are calculated using the 'physical' value $\sqrt{\sigma} = 427$ MeV for the string tension. The separation is the total number of updates (Cabibbo–Marinari or over-relaxation) separating the configurations. $\langle U \rangle$ is the average link $\sum_{x,\mu} \text{Re} \, \text{Tr} \, U_\mu(x)/(4V N_c)$

$[\hat{q}_x, \hat{q}_y, \hat{q}_z, \hat{q}_t]$	Components	Theoretical prediction		This simulation	
		Using $\hat{q}$	Using q	Using A	Using A'
[2,1,0,0]	(1,1)/(1,2)	-0.5	-0.509796	-0.509796	-0.519783
	(1,1)/(2,2)	0.25	0.259892	0.259892	0.259892
	(1,1)/(3,3)	0.2	0.206281	0.204(8)	0.204(8)
	(1,1)/(4,4)	0.2	0.206281	0.199(9)	0.199(9)
	(1,2)/(2,2)	-0.5	-0.509796	-0.509796	-0.5
	(1,2)/(3,3)	-0.4	-0.404634	-0.40(2)	-0.38(2)
[4,1,0,0]	(1,1)/(1,2)	-0.25	-0.275899	-0.275899	-0.331821
	(1,1)/(2,2)	0.0625	0.0761205	0.0761205	
	(1,2)/(2,2)	-0.25	-0.275899	-0.275899	-0.229402
	(1,2)/(3,3)	-0.2353	-0.256383	-0.277(12)	-0.231(10)
[4,2,0,0]	(1,1)/(1,2)	-0.5	-0.541196	-0.541196	-0.585786
	(1,1)/(2,2)	0.25	0.292893	0.292893	
	(1,1)/(3,3)	0.2	0.226541	0.22(1)	
	(1,2)/(2,2)	-0.5	-0.541196	-0.541196	-0.5
[2,1,1,0]	(1,1)/(1,2)	-1	-1.01959	-1.01(2)	-1.03(2)
	(1,1)/(2,2)	0.4	0.412562	0.411(15)	
	(1,1)/(3,3)	0.4	0.412562	0.418(14)	
	(1,2)/(2,2)	-0.4	-0.404634	-0.407(10)	-0.398(11)
[4,2,1,0]	(1,1)/(1,2)	-0.625	-0.681848	-0.678(9)	-0.743(10)
	(1,1)/(2,2)	0.2941	0.342911	0.339(7)	
	(1,1)/(2,3)	-2.5	-2.47137	-2.3(4)	-2.5(5)
	(1,3)/(3,3)	-0.2	-0.213397	-0.208(10)	-0.187(11)
[4,2,1,1/3]	(1,1)/(1,2)	-0.6389	-0.697656	-0.695(9)	-0.750(10)
	(1,1)/(2,2)	0.2987	0.348094	0.348(8)	
	(1,1)/(4,4)	0.2434	0.275796	0.288(13)	
	(1,2)/(2,2)	-0.4675	-0.498947	-0.500(7)	-0.464(7)
	(1,3)/(2,2)	-0.2338	-0.254361	-0.25(2)	-0.20(2)

TABLE II. Tensor structure for the small lattice. $\hat{q}$ is in units of $2\pi/L_s$, where L_s is the spatial length of the lattice. The theoretical predictions are the values for the ratios one obtains from (5.1), and from (5.1) with $q \to \hat{q}$. The numbers in brackets are the statistical uncertainties in the last digit(s). Where no error is quoted, the statistical uncertainty is less than 10^{-6}. The values obtained using the asymmetric gluon field definition A' are only shown where they differ from the value using A.

| $[\hat{q}_x, \hat{q}_y, \hat{q}_z, \hat{q}_t]$ | Components | Theoretical prediction | | This simulation |
		Using $\hat{q}$	Using q	Using A
[2,1,0,0]	(1,1)/(1,2)	-0.5	-0.502419	-0.502419
	(1,1)/(2,2)	0.25	0.252425	0.252425
	(1,1)/(3,3)	0.2	0.201549	0.217(13)
	(1,2)/(3,3)	-0.4	-0.401157	-0.43(3)
[8,4,0,0]	(1,1)/(1,2)	-0.5	-0.541196	-0.541196
	(1,1)/(2,2)	0.25	0.292893	0.292893
	(1,1)/(3,3)	0.2	0.226541	0.21(1)
[8,4,2,0]	(1,1)/(1,2)	-0.625	-0.681848	-0.691(12)
	(1,1)/(2,2)	0.2941	0.342911	0.351(11)
	(1,2)/(2,2)	-0.4706	-0.502914	-0.508(9)
	(1,3)/(3,3)	-0.2	-0.213397	-0.223(15)
[8,2,1,1/2]	(1,1)/(1,2)	-0.3281	-0.362996	-0.360(6)
	(1,1)/(4,4)	0.07609	0.0914336	0.085(4)
	(1,2)/(2,2)	-0.2452	-0.269425	-0.265(5)
	(1,3)/(2,2)	-0.1226	-0.135364	-0.134(11)

TABLE III. Tensor structure for the large lattice. $\hat{q}$ is given in units of $2\pi/L_s$, where L_s is the spatial length of the lattice. Since the spatial length of this lattice is twice that of the small lattice, the values for $\hat{q}$ must be multiplied by 2 when comparing these values with those of Table II.

$[\hat{q}_x, \hat{q}_y, \hat{q}_z, \hat{q}_t]$	Components	Theoretical prediction		This simulation	
		Using $\hat{q}$	Using q	Using A	Using A'
[2,1,0,0]	(1,1)/(1,2)	-0.5	-0.504314	-0.504315	-0.508666
	(1,1)/(2,2)	0.25	0.254333	0.254333	
	(1,2)/(2,2)	-0.5	-0.504314	-0.504315	-0.5
	(1,2)/(3,3)	-0.4	-0.402058	-0.405(14)	-0.402(14)
[6,1,0,0]	(1,1)/(1,2)	-0.1667	-0.184592	-0.184592	-0.232673
	(1,2)/(2,2)	-0.1667	-0.184592	-0.184592	-0.146447
	(1,2)/(3,3)	-0.1622	-0.178509	-0.183(6)	-0.145(5)
[6,3,0,0]	(1,1)/(1,2)	-0.5	-0.541196	-0.541196	-0.585786
	(1,1)/(2,2)	0.25	0.292893	0.292893	
	(1,1)/(3,3)	0.2	0.226541	0.226(7)	
	(1,2)/(2,2)	-0.5	-0.541196	-0.541196	-0.5
[6,3,1,0]	(1,1)/(1,2)	-0.5556	-0.604157	-0.605(4)	-0.655(4)
	(1,1)/(2,2)	0.2703	0.316193	0.318(4)	
	(1,3)/(3,3)	-0.1333	-0.142774	-0.149(8)	-0.118(8)
[6,3,1,1]	(1,1)/(1,2)	-0.6111	-0.667118	-0.666(7)	-0.717(8)
	(1,1)/(4,4)	0.2391	0.27208	0.270(9)	
	(1,2)/(2,2)	-0.4737	-0.506668	-0.500(5)	-0.464(5)
	(1,3)/(2,2)	-0.1579	-0.172815	-0.188(14)	-0.147(12)

TABLE IV. Tensor structure for the fine lattice

$[\hat{q}_x, \hat{q}_y, \hat{q}_z, \hat{q}_t]$	Components	Ratio according to (5.1)	This simulation
[1,0,0,0]	(2,2)/(3,3)	1	1.01(5)
	(2,2)/(4,4)	1	1.24(6)
	(3,3)/(4,4)	1	1.23(6)
[0,0,1,0]	(1,1)/(4,4)	1	1.25(5)
	(2,2)/(4,4)	1	1.32(6)
[1,0,0,1/3]	(1,1)/(2,2)	0.101034	0.083(4)
	(2,2)/(4,4)	1.11239	1.35(7)
	(3,3)/(4,4)	1.11239	1.36(6)
[1,0,0,2/3]	(1,1)/(2,2)	0.309218	0.275(13)
	(2,2)/(4,4)	1.44763	1.63(7)
	(3,3)/(4,4)	1.44763	1.61(7)
[1,1,0,0]	(3,3)/(4,4)	1	1.10(5)
[1,0,1,0]	(2,2)/(4,4)	1	1.17(6)
[0,1,1,0]	(1,1)/(4,4)	1	1.05(5)
[1,0,0,1]	(1,1)/(4,4)	1	1
	(2,2)/(1,1)	2	1.98(10)
	(3,3)/(4,4)	2	2.22(10)
[0,0,1,1]	(1,1)/(3,3)	2	2.25(10)
	(1,1)/(4,4)	2	2.25(10)
	(2,2)/(4,4)	2	2.13(10)

TABLE V. Tensor structure for low momentum values on the small lattice.

$[\hat{q}_x, \hat{q}_y, \hat{q}_z, \hat{q}_t]$	Components	Ratio according to (5.1)	This simulation
[1,0,0,0]	(2,2)/(3,3)	1	0.95(3)
	(2,2)/(4,4)	1	1.20(4)
	(3,3)/(4,4)	1	1.26(4)
[2,0,0,0]	(2,2)/(3,3)	1	1.00(4)
	(2,2)/(4,4)	1	1.08(4)
	(3,3)/(4,4)	1	1.07(4)
[1,0,0,1/2]	(1,1)/(2,2)	0.200687	0.170(6)
	(1,1)/(3,3)	0.200687	0.187(6)
	(2,2)/(4,4)	1.25107	1.47(5)
	(3,3)/(4,4)	1.25107	1.34(4)

TABLE VI. Tensor structure for low momentum values on the fine lattice.

$[\hat{q}_x, \hat{q}_y, \hat{q}_z, \hat{q}_t]$	Components	Ratio according to (5.1)	This simulation
[1,0,0,0]	(2,2)/(3,3)	1	0.97(5)
	(2,2)/(4,4)	1	1.13(6)
	(3,3)/(4,4)	1	1.17(6)
[0,1,0,0]	(1,1)/(4,4)	1	1.13(7)
	(3,3)/(4,4)	1	1.17(8)
[0,0,1,0]	(1,1)/(4,4)	1	1.05(6)
	(2,2)/(4,4)	1	1.08(6)
[2,0,0,0]	(2,2)/(3,3)	1	0.97(7)
	(2,2)/(4,4)	1	1.10(7)
	(3,3)/(4,4)	1	1.14(6)
[0,2,0,0]	(1,1)/(4,4)	1	1.09(6)
	(3,3)/(4,4)	1	1.02(7)
[1,0,0,1/2]	(1,1)/(2,2)	0.200386	0.182(10)
	(1,4)/(2,2)	-0.400289	-0.36(2)
	(2,2)/(4,4)	1.2506	1.37(7)
	(3,3)/(4,4)	1.2506	1.34(7)
[0,0,1,1/2]	(3,3)/(1,1)	0.200386	0.196(10)
	(3,4)/(1,1)	-0.400289	0.39(2)
	(1,1)/(4,4)	1.2506	1.27(7)
	(2,2)/(4,4)	1.2506	1.33(8)

TABLE VII. Tensor structure for the large lattice, low values of $\hat{q}$. Note that $\hat{q}$ is given in units of $2\pi/L_s$, so that eg. $\hat{q} = [2, 0, 0, 0]$ corresponds to $\hat{q} = [1, 0, 0, 0]$ for the small lattice.

Components	Small lattice	Large lattice	Fine lattice
(1,1)/(2,2)	0.93(6)	1.05(8)	0.98(4)
(1,1)/(3,3)	1.03(6)	0.94(8)	0.98(4)
(2,2)/(3,3)	1.10(7)	0.90(8)	1.00(5)
(1,1)/(4,4)	3.09(19)	1.42(11)	2.06(9)
(2,2)/(4,4)	3.31(20)	1.35(12)	2.10(10)
(3,3)/(4,4)	3.00(18)	1.51(11)	2.09(9)

TABLE VIII. Ratios of the diagonal components of $D_{\mu\nu}(q = 0)$ for all three lattices.

Lattice	q_{min}, q_{max} (a^{-1})		q_{min}, q_{max} (GeV)		No. of points	χ^2/N_{df}	Z	Λa	Λ (GeV)
$\beta = 6.0$	1.47	2.78	2.72	5.14	27	1.48	2.140	0.399	0.752
$16^3 \times 48$	1.59	2.78	2.94	5.14	25	1.43	2.162	0.387	0.730
	2.12	2.78	3.92	5.14	15	1.13	2.151	0.394	0.743
$\beta = 6.0$	1.53	2.83	2.83	5.23	69	1.42	2.159	0.387	0.729
$32^3 \times 64$	1.53	2.76	2.83	5.10	67	1.34	2.157	0.387	0.730
	2.10	2.76	3.89	5.10	29	1.28	2.184	0.373	0.703
	2.12	2.76	3.91	5.10	27	1.10	2.220	0.354	0.667
	2.12	2.83	3.91	5.23	29	1.29	2.223	0.350	0.660
$\beta = 6.2$	1.09	2.83	2.83	7.36	53	1.33	2.286	0.275	0.726
$24^3 \times 48$	1.09	2.44	2.83	6.34	43	1.30	2.274	0.279	0.736
	1.09	2.00	2.83	5.20	29	0.81	2.222	0.297	0.782
	1.49	2.83	3.87	7.36	41	1.02	2.341	0.253	0.668
	1.49	2.00	3.87	5.20	17	0.78	2.212	0.301	0.793

TABLE IX. Parameter values and χ^2 for fits to the asymptotic form (5.2). Note that in this table, Z is actually $Z_3(\mu, a)Z$ of Eq. (5.2). The fits are to data surviving the cylindrical and cone cuts, except for the large lattice, where only the cylindrical cut has been applied.

Model	$\chi^2_{\text{all}}/N_{df}$	$\chi^2_{\text{min}}/N_{df}$	Range (qa)	N_{fit}	$\chi^2_{\text{IR}}/N_{df}$	Range (qa)	N_{fit}
Gribov	827	0.31	0.28–0.39	5			
Stingl	838	0.44	0.28–0.45	8	1.03	0.28–0.49	10
Marenzoni	163	0.79	1.11–1.47	24	1.20	0.20–0.59	18
Cornwall I	50	0.67	0.99–1.47	30	1.01	0.20–0.62	20
Cornwall II	89	0.49	1.26–1.47	14	0.69	0.28–0.45	8
Cornwall III	38	0.64	1.13–1.33	23	1.05	0.20–0.48	11

TABLE X. χ^2 per degree of freedom for fits to the models (5.8)–(5.13). χ^2_{all} is the χ^2 for the maximum available fitting range. χ^2_{min} corresponds to the minimum value obtained for χ^2/N_{df}, "Range" is the corresponding fitting range, and N_{fit} is the number of points included in that range. χ^2_{IR} refers to the widest fitting range starting in the deep infrared (point 2 or 4) where $\chi^2/N_{df} \lesssim 1$.

Model	χ^2/N_{df}	Z	A	M	α or Λ
Marenzoni	163	2.41^{+0}_{-12}		0.14^{+4}_{-14}	0.29^{+6}_{-2}
Cornwall I	50.3	6.5^{+7}_{-9}		0.24^{+3}_{-16}	0.27^{+7}_{-7}
Model C	13.9	2.55^{+147}_{-0}	1.07^{+8}_{-97}	0.23^{+1}_{-22}	0.53^{+4}_{-29}
Model A	1.40	2.01^{+4}_{-5}	9.84^{+10}_{-86}	0.54^{+5}_{-5}	2.17^{+11}_{-19}
Model A$_2$	2.16	2.03^{+2}_{-1}	8.85^{+44}_{-0}	0.51^{+1}_{-2}	
Model B	12.1	2.09^{+0}_{-21}	2.29^{+17}_{-39}	0.38^{+23}_{-1}	1.09^{+46}_{-7}

TABLE XI. Parameter values in lattice units for fits of models (5.10)–(5.16). The values quoted are for fits to the entire set of data. The errors denote the uncertainty in the last digit(s) of the parameter values which results from varying the fitting range. The fitting ranges considered when evaluating the uncertainties are those with a minimum of 40 points included and with the minimum value for qa no larger than 0.99 (point number 40), corresponding to $q_{\min} \leq 1.86$ GeV. For Model C, the fitting ranges have been restricted to minimum values for qa no larger than 0.62 (point number 20), in order to obtain meaningful uncertainties. Model A$_2$ denotes Model A with α fixed to 2. Recall that the inverse lattice spacing for this lattice is 1.885 GeV.

This figure "fig13.gif" is available in "gif" format from:

http://arXiv.org/ps/hep-lat/9811027v2

This figure "fig14.gif" is available in "gif" format from:

http://arXiv.org/ps/hep-lat/9811027v2